Available online at www.sciencedirect.com
SCIENCE DIRECT®
Continental Shelf Research 24 (2004) 2133–2148
CONTINENTAL SHELF RESEARCH
www.elsevier.com/locate/csr

Hydrostatic and non-hydrostatic studies of gravitational adjustment over a slope

Yngve Heggelund[a,*], Frode Vikebø[b], Jarle Berntsen[c,1], Gunnar Furnes[d]

[a]*Christian Michelsen Research, P.O. Box 6031 Postterminalen, N-5892 Bergen, Norway*
[b]*Institute of Marine Research, P.O. Box 1870 Nordnes, N-5817 Bergen, Norway*
[c]*Department of Mathematics, University of Bergen, Johs. Bruns gt 12, N-5008 Bergen, Norway*
[d]*Norsk Hydro, E & P Research Centre, P.O. Box 7190, N-5020 Bergen, Norway*

Available online 8 September 2004

Abstract

In many numerical ocean models, the hydrostatic approximation is made. This approximation causes a considerable saving in computing time. However, for phenomena involving large vertical speeds, for many small scale phenomena, and in areas with weak stratification, the approximation becomes questionable. In this report, a σ-coordinate hydrostatic C-grid model is extended to include non-hydrostatic dynamics. The test cases involve gravitational adjustment of a downslope flow. The first test case has a simplified slope profile and no ambient stratification in the deep basin. The second test case has ambient stratification and more realistic topography. The differences between hydrostatic and non-hydrostatic simulations are described and discussed. It is shown that the shapes of the head and the body of density driven plumes are better preserved in the non-hydrostatic experiments. The wave propagation away from the plume head is considerably reduced when including non-hydrostatic effects.
© 2004 Elsevier Ltd. All rights reserved.

Keywords: Ocean circulation; Shelf dynamics; Hydrostatic pressure; Density flow

1. Introduction

With improvements in computing power, it becomes possible to use increasingly finer meshes in numerical ocean models. At some limit, depending on the problem studied, the hydrostatic assumption made in most ocean models will no longer be a good approximation for all the time and length scales resolvable by the model. Further refinements of the grid should therefore include non-hydrostatic physics. Based on scale analysis, see Marshall et al. (1997b), the following criterion may be used to check the validity of the hydrostatic approximation:

$$n = \frac{\gamma^2}{R_i} \ll 1, \tag{1}$$

*Corresponding author.
E-mail addresses: yngve.heggelund@cmr.no (Y. Heggelund), frovik@imr.no (F. Vikebø), jarle.berntsen@mi.uib.no (J. Berntsen), gunnar.furnes@hydro.com (G. Furnes).
[1]Also for correspondence.

0278-4343/$ - see front matter © 2004 Elsevier Ltd. All rights reserved.
doi:10.1016/j.csr.2004.07.005

where n is the non-hydrostatic parameter, $\gamma = h/L$ is the ratio of the vertical length scale to the horizontal length scale and $R_i = N^2h^2/U^2$ is the Richardson number. (N is the Brunt–Väisälä frequency, U is the horizontal velocity scale.) They state that for ocean modelling, the hydrostatic assumption may begin to break down for phenomena of horizontal length scale somewhere between 1 and 10 km, depending on the strength of the stratification.

Several numerical models have been built that includes non-hydrostatic physics, see Mahadevan et al. (1996a, b), Stansby and Zhou (1998), and Marshall et al. (1997b, a). Convection in the ocean is recently studied with non-hydrostatic z-coordinate ocean models. See Legg et al. (1998) and Legg and McWilliams (2000, 2001). Lamb (1994) applied a terrain following, non-hydrostatic, rigid lid ocean model using projection of the flow field onto the divergence free part to study internal wave generation. This paper describes a way to extend a σ-coordinate free surface general circulation ocean model using splitting of the flow field into the depth averaged part and the deviation from the depth average, to include non-hydrostatic physics through a velocity correcting pressure term. A similar extension for an atmospheric model has been described in Dudhia (1993), and in Marshall et al. (1997b) for an z-coordinate ocean model. The velocity correction is implemented so that it can be switched on and off by the user, which makes it easy to study the effect of non-hydrostatic physics on a given test case.

The test cases presented here are investigations of the flow of dense water down a steep topographic slope in the absence of rotation, as posed in Haidvogel and Beckmann (1999). Locally, near the density front, the gradient of the density works as a destabilising force, contrary to many ocean circulation phenomena. The flow will therefore accelerate until the acceleration is balanced by entrainment. The vertical acceleration terms may therefore be significant for gravity plumes. Understanding of this problem can be important for example when studying phenomena at the Norwegian continental shelf edge. The problem is also interesting for larger scale ocean circulation studies. Especially for the North Atlantic, where inflow and outflow of dense water through narrow and steep straits and subsequent downslope flow and mixing can be important processes in the production of North Atlantic Deep Water.

Section 2 gives a brief overview of the basic equations, the σ-coordinate system and the numerical implementation of the model. In Section 3 a derivation of the non-hydrostatic pressure correction equation is presented, and Section 4 consists of descriptions and results from test cases. In the discussion part, the main findings are summarised and presented in a broader context.

2. The basic equations

The basic equations are the Reynolds averaged momentum equations where the Boussinesq approximation has been used (the density differences are neglected unless the density is multiplied by gravity)

$$\frac{\partial U}{\partial t} + \vec{U}\cdot\nabla U + W\frac{\partial U}{\partial z} - fV = -\frac{1}{\rho_0}\frac{\partial p}{\partial x} + F_x, \quad (2)$$

$$\frac{\partial V}{\partial t} + \vec{U}\cdot\nabla V + W\frac{\partial V}{\partial z} + fU = -\frac{1}{\rho_0}\frac{\partial p}{\partial y} + F_y, \quad (3)$$

$$\frac{\partial W}{\partial t} + \vec{U}\cdot\nabla W + W\frac{\partial W}{\partial z} = -\frac{1}{\rho_0}\frac{\partial p}{\partial z} - \frac{\rho g}{\rho_0} + F_z, \quad (4)$$

where $\vec{U}$ and ∇U are the horizontal velocity vector and horizontal gradient operator, respectively, W the vertical velocity, f the Coriolis parameter, p the pressure, ρ the density, ρ_0 the reference density, and g the gravity. F_x, F_y and F_z are the horizontal and vertical viscosity/eddy-viscosity terms.

If the hydrostatic approximation is made, all terms in the vertical momentum equation except the pressure term and the gravity term are neglected. The third equation is then reduced to

$$\frac{\partial p}{\partial z} = -\rho g. \quad (5)$$

The equation of continuity is

$$\frac{\partial U}{\partial x} + \frac{\partial V}{\partial y} + \frac{\partial W}{\partial z} = 0. \quad (6)$$

The conservation equation for density(ρ) is

$$\frac{\partial \rho}{\partial t} + \vec{U} \cdot \nabla \rho + W \frac{\partial \rho}{\partial z} = \frac{\partial}{\partial z}\left(K_H \frac{\partial \rho}{\partial z}\right) + F_\rho, \qquad (7)$$

where F_ρ is the horizontal diffusivity and K_H the vertical diffusivity.

The numerical sigma-coordinate ocean model applied in the present studies is described in Berntsen (2000) and is available from www.mi.uib.no/BOM/. See also Berntsen and Svendsen (1999), Avlesen et al. (2001), Eliassen et al. (2001) and Berntsen (2002). The finite difference grid is staggered, and the Arakawa C-grid (Mesinger and Arakawa, 1976) has been used, see Fig. 1 where the positions of all the 3D fields are shown. The water elevation and the depth integrated velocities (the 2D fields) are given at cell centers and cell interfaces respectively. The governing equations are basically the same as for the Princeton Ocean Model (POM) (Blumberg and Mellor, 1987 and Mellor, 1996), but the numerical methods are different. For advection of momentum and density a TVD-scheme with a superbee limiter described in Yang and Przekwas (1992) is applied. The model is mode split with a method similar to the splitting described in Berntsen et al. (1981) or more recently in Kowalik and Murty (1993). That is: $U = U_{2D} + U'$, where U_{2D} is the depth averaged velocity and U' the deviation from the average. The solution is propagated in time using single time step methods. For the depth-integrated momentum and continuity equations the forward–backward method is applied. After the depth-integrated velocities at the new time step are estimated, the deviation U' is also propagated in time to the new time step under the hydrostatic assumption and $U^{n+1} = U_{2D}^{n+1} + U'^{,n+1}$. In non-hydrostatic mode, effects of the non-hydrostatic pressure corrections are included when estimating $U'^{,n+1}$.

In all experiments reported here the model is run with zero horizontal diffusivity on the density field. The horizontal viscosity, A_M, is computed according to Smagorinsky (1963). The constant C_M in the Smagorinsky model, see Mellor (1996), is set to 0.2 in both test cases. In the vertical the Mellor–Yamada 2-1/2 level scheme (Mellor and Yamada (1982)) is applied to parameterise sub-grid-scale processes. The internal pressure is estimated with the second order central difference scheme as in POM.

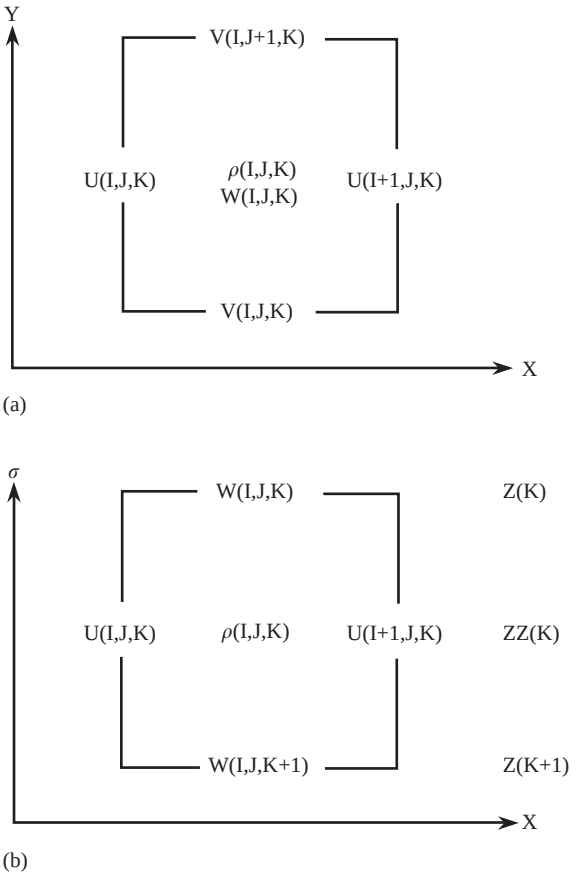

Fig. 1. The location of 3D variables in the C-grid. Z is the σ-coordinate at the cell interface, and ZZ is the σ-coordinate at the cell center. (a) Horizontal view. (b) Vertical view.

The basic equations are transformed into a σ-coordinate system. This is a bottom and surface following coordinate system that has the property that the bottom always has the σ-coordinate -1 and the free surface always has the σ-coordinate 0.

The transformation from the Cartesian coordinate system (x, y, z, t) to the σ-coordinate system (x^*, y^*, σ, t^*) is given by

$$x^* = x y^* = y \sigma = \frac{z - \eta}{\eta + H} t^* = t,$$

where $\eta(x, y, t)$ is the surface elevation and $H(x, y)$ is the depth measured from the surface at rest.

3. The pressure-correction equation

The non-hydrostatic correction is accomplished by introducing a pressure-correction term p', where p' is the deviation from the hydrostatic pressure.

In both the hydrostatic and the non-hydrostatic model, the change in surface elevation η exactly balances the gradient of the horizontal fluxes. The new η is found in the calculation of the 2D external mode, where it is balanced against depth averaged velocities $(U_{2D}^{n+1}, V_{2D}^{n+1})$. Two new 3D velocities $(U_{ADV}^{n*}, V_{ADV}^{n*})$ with the same vertical average as $(U_{2D}^{n+1}, V_{2D}^{n+1})$, and the same vertical variation as the total velocities (U^n, V^n) are then defined.

In the hydrostatic model, no further corrections to U_{ADV}^{n*} and V_{ADV}^{n*} are made, so these variables can be renamed U_{ADV}^{n+1} and V_{ADV}^{n+1} and the vertical velocity w^{n+1} is calculated using the equation of continuity, i.e.

$$w^{n+1}(\sigma) = \int_{\sigma}^{0} \left(\frac{\partial (U_{ADV} D)^{n+1}}{\partial x} + \frac{\partial (V_{ADV} D)^{n+1}}{\partial y} \right) d\sigma - \sigma \frac{\partial \eta}{\partial t}, \tag{8}$$

using the fact that $w(0) = 0$. D is the dynamic depth ($D = H + \eta$). Volume conservation in every cell is maintained, and U_{ADV}^{n+1}, V_{ADV}^{n+1}, w^{n+1}, η^n and η^{n+1} can therefore be used for advection of scalar fields.

In the non-hydrostatic model, the calculation of the vertical velocity is postponed until a pressure correction p' is found. The gradient of this pressure term gives corrections to the horizontal velocities, and thus also to the vertical velocity w through Eq. (8).

Following ideas from industrial computational fluid dynamics described for instance in Patankar (1980), we may consider the terms of the equations describing a balance between the acceleration terms and the pressure terms first, and derive an equation for the non-hydrostatic pressure corrections. Remaining terms are treated separately numerically. In the Cartesian coordinate system this can be written

$$\frac{dU}{dt} = -\frac{1}{\rho_0} \frac{\partial p}{\partial x}, \tag{9}$$

$$\frac{dV}{dt} = -\frac{1}{\rho_0} \frac{\partial p}{\partial y}, \tag{10}$$

$$\frac{dW}{dt} = -\frac{1}{\rho_0} \frac{\partial p}{\partial z} - \frac{\rho g}{\rho_0}, \tag{11}$$

where $\frac{d}{dt} = \frac{\partial}{\partial t} + \vec{U} \cdot \nabla$ is the total derivative, $\vec{U}$ is the 3D velocity vector and ∇ is the 3D gradient operator.

We split the pressure into three parts

$$p = p_G + p_\eta + p', \tag{12}$$

where

$$p_G = g \int_{z}^{0} \rho(z')\, dz' \tag{13}$$

and

$$p_\eta = g \rho_0 \eta \tag{14}$$

and p' is the non-hydrostatic pressure-correction term to be calculated. p_G balances the gravity term in the vertical, and p_η is independent of z. These two pressure terms are included in the hydrostatic model. The horizontal advection terms are also included in the hydrostatic model.

The equations in sigma-coordinates for the non-hydrostatic pressure correction then become

$$\frac{\partial UD}{\partial t} = -\frac{D}{\rho_0} \frac{\partial p}{\partial x} + \frac{1}{\rho_0} \frac{\partial p}{\partial \sigma} \left(\frac{\partial \eta}{\partial x} + \sigma \frac{\partial D}{\partial x} \right), \tag{15}$$

$$\frac{\partial VD}{\partial t} = -\frac{D}{\rho_0} \frac{\partial p}{\partial y} + \frac{1}{\rho_0} \frac{\partial p}{\partial \sigma} \left(\frac{\partial \eta}{\partial y} + \sigma \frac{\partial D}{\partial y} \right), \tag{16}$$

$$\frac{\partial WD}{\partial t} = -\frac{1}{\rho_0} \frac{\partial p}{\partial \sigma}. \tag{17}$$

Primes and asterisks are deleted to simplify notation. We also require that the velocity corrections satisfy the equation of continuity

$$\frac{\partial UD}{\partial x} + \frac{\partial VD}{\partial y} + \frac{\partial w}{\partial \sigma} + \frac{\partial \eta}{\partial t} = 0. \tag{18}$$

With the vertical velocity transformation

$$w = D \frac{d\sigma}{dt} = W - U \left(\sigma \frac{\partial D}{\partial x} + \frac{\partial \eta}{\partial x} \right) - V \left(\sigma \frac{\partial D}{\partial y} + \frac{\partial \eta}{\partial y} \right) - \left(\sigma \frac{\partial D}{\partial t} + \frac{\partial \eta}{\partial t} \right), \tag{19}$$

this is a closed set of equations. The change in surface elevation η is balanced by the horizontal fluxes. The non-hydrostatic pressure will not change the vertical averaged horizontal fluxes into a water column, so η will not be changed by the non-hydrostatic pressure.

The σ-coordinate system is not an orthogonal coordinate system, and this is the reason for the $\partial p/\partial\sigma$-terms on the right-hand side of the horizontal momentum equations. In a z-coordinate model like the MIT-model, see Marshall et al. (1997a), the solution matrices get a nice structure with six off-diagonal entries. The techniques for solving linear systems with this structure are well established. The $\partial p/\partial\sigma$-terms destroy this structure, and create a stronger coupling between the equations. This may lead to a very CPU-intensive code. Our strategy to handle this problem is to solve a simplified system of equations iteratively. The system of equations to be solved in each iteration step will have the same structure as for a z-coordinate model. However, it is necessary to recompute the $\partial p/\partial\sigma$ terms for each iteration, and include the effect as a forcing to the simplified system of equations.

Defining the discretized pressure in cell centers, we can write the equations governing p, in finite difference notation, as

$$\frac{U_{\mathrm{CORR}}{}_{ijk}^{n+1} D_{U}{}_{ij}^{n+1}}{\Delta t} = -\frac{D_{U}{}_{ij}^{n+1}}{\rho_0}\frac{p_{ijk}^{n+1}-p_{i-1jk}^{n+1}}{\Delta x} + \frac{U_{\mathrm{CORR2}}{}_{ijk}^{n+1} D_{U}{}_{ij}^{n+1}}{\Delta t}, \tag{20}$$

$$\frac{V_{\mathrm{CORR}}{}_{ijk}^{n+1} D_{V}{}_{ij}^{n+1}}{\Delta t} = -\frac{D_{V}{}_{ij}^{n+1}}{\rho_0}\frac{p_{ijk}^{n+1}-p_{ij-1k}^{n+1}}{\Delta y} + \frac{V_{\mathrm{CORR2}}{}_{ijk}^{n+1} D_{V}{}_{ij}^{n+1}}{\Delta t}, \tag{21}$$

$$\frac{W_{ijk}^{n+1}-W_{ijk}^{n}}{\Delta t} = -\frac{1}{D_{ij}^{n+1}\rho_0}\frac{p_{ijk-1}^{n+1}-p_{ijk}^{n+1}}{\Delta\tilde{\sigma}_{k-1}}, \tag{22}$$

$$\frac{(U_{\mathrm{ADV}}D_U)_{i+1jk}^{n+1}-(U_{\mathrm{ADV}}D_U)_{ijk}^{n+1}}{\Delta x} + \frac{(V_{\mathrm{ADV}}D_V)_{ij+1k}^{n+1}-(V_{\mathrm{ADV}}D_V)_{ijk}^{n+1}}{\Delta y} + \frac{w_{ijk}^{n+1}-w_{ijk+1}^{n+1}}{\Delta\sigma_k} + \frac{\eta_{ij}^{n+1}-\eta_{ij}^{n}}{\Delta t} = 0, \tag{23}$$

where $U_{\mathrm{CORR}}^{n+1} = U_{\mathrm{ADV}}^{n+1} - U_{\mathrm{ADV}}^{n*}$ and $V_{\mathrm{CORR}}^{n+1} = V_{\mathrm{ADV}}^{n+1} - V_{\mathrm{ADV}}^{n*}\cdot U_{\mathrm{CORR2}}^{n+1}$ and V_{CORR2}^{n+1} are second-order discretizations of the terms involving $\partial p/\partial\sigma$ in the horizontal velocity equations. The term U_{CORR2}^{n+1} thus becomes

$$U_{\mathrm{CORR2}}{}_{ijk}^{n+1} = \frac{\Delta t}{2D_{U}{}_{ij}^{n+1}\rho_0}\frac{p_{i-1jk-1}^{n+1}-p_{i-1jk+1}^{n+1}+p_{i1jk-1}^{n+1}-p_{i1jk+1}^{n+1}}{\Delta\tilde{\sigma}_{k-1}+\Delta\tilde{\sigma}_k} \times\left(\frac{\eta_{ij}^{n+1}-\eta_{i-1j}^{n+1}}{\Delta x}+\sigma\frac{D_{ij}^{n+1}-D_{i-1j}^{n+1}}{\Delta x}\right), \tag{24}$$

where D_U, D_V and D are the dynamic depths in U-points, V-points and cell centers, respectively, $\Delta\sigma_k$ is the vertical distance between cell interfaces at level k, and $\Delta\tilde{\sigma}_k$ is the vertical distance between cell centers at level k. The term V_{CORR2}^{n+1} is computed similarly.

Using Eq. (19), Eq. (22) can be rewritten in terms of the σ-coordinate velocity w

$$\frac{w_{ijk}^{n+1}-w_{ijk}^{n*}}{\Delta t}+\frac{r_{ijk}^{n+1}-r_{ijk}^{n*}}{\Delta t} = -\frac{1}{D_{ij}^{n+1}\rho_0}\frac{p_{ijk-1}^{n+1}-p_{ijk}^{n+1}}{\Delta\tilde{\sigma}_{k-1}}, \tag{25}$$

where $r_{ijk}^{n+1}-r_{ijk}^{n*} = \overline{U}_{\mathrm{CORR}}{}_{ijk}^{n+1}\frac{\eta_{i+1jk}-\eta_{i-1jk}}{2\Delta x}+\overline{V}_{\mathrm{CORR}}{}_{ijk}^{n+1}\frac{\eta_{ij+1k}-\eta_{ij-1k}}{2\Delta y}$, where $\overline{U}_{\mathrm{CORR}}$ and $\overline{V}_{\mathrm{CORR}}$ are averaged to w points (see Fig. 1). $r_{ijk}^{n+1}-r_{ijk}^{n*}$ is updated during the pressure iteration. It is only calculated at w-points in the interior of the domain, in order to avoid introduction of erroneous fluxes through the surface or the bottom.

Eqs. (20), (21), (23) and (25) are combined in Eq. (26) to give a system of equations for the dynamic pressure correction p at time step $n+1$. v indicates the iteration number.

$$A_{ijk}^{n+1}p_{i-1jk}^{n+1,v}+B_{ijk}^{n+1}p_{i+1jk}^{n+1,v}+C_{ijk}^{n+1}p_{ij-1k}^{n+1,v}+D_{ijk}^{n+1}p_{ij+1k}^{n+1,v} + E_{ijk}^{n+1}p_{ijk-1}^{n+1,v}+F_{ijk}^{n+1}p_{ijk+1}^{n+1,v}+G_{ijk}^{n+1}P_{ijk}^{n+1,v} = \frac{U_{\mathrm{ADV}}{}_{i+1jk}^{n*}D_{U}{}_{i+1j}^{n+1}-U_{ADV}{}_{ijk}^{n*}D_{U}{}_{ij}^{n+1}}{\Delta x}$$

$$+\frac{V_{\mathrm{ADV}}{}^{n*}_{ij+1k}D_V{}^{n+1}_{ij+1}-V_{\mathrm{ADV}}{}^{n*}_{ijk}D_V{}^{n+1}_{ij}}{\Delta y}$$
$$+\frac{w^n_{ijk}-w^n_{ijk+1}}{\Delta\sigma_k}+\frac{\eta^{n+1}_{ij}-\eta^n_{ij}}{\Delta t}$$
$$-\frac{(r^{n+1}_{ijk}-r^{n*}_{ijk})-(r^{n+1}_{ijk+1}-r^{n*}_{ijk+1})}{\Delta\sigma_k}$$
$$+\frac{U_{\mathrm{CORR2}}{}^{n+1,v-1}_{i+1jk}D_U{}^{n+1}_{i+1j}-U_{\mathrm{CORR2}}{}^{n+1,v-1}_{ijk}D_U{}^{n+1}_{ij}}{\Delta x}$$
$$+\frac{V_{\mathrm{CORR2}}{}^{n+1,v-1}_{ij+1k}D_V{}^{n+1}_{i+1j}-V_{\mathrm{CORR2}}{}^{n+1,v-1}_{ijk}D_V{}^{n+1}_{ij}}{\Delta y}, \tag{26}$$

where

$$A^{n+1}_{ijk}=\frac{\Delta t}{\rho_0\Delta x^2}D_U{}^{n+1}_{ij}, \tag{27}$$

$$B^{n+1}_{ijk}=\frac{\Delta t}{\rho_0\Delta x^2}D_U{}^{n+1}_{i+1j}, \tag{28}$$

$$C^{n+1}_{ijk}=\frac{\Delta t}{\rho_0\Delta y^2}D_V{}^{n+1}_{ij}, \tag{29}$$

$$D^{n+1}_{ijk}=\frac{\Delta t}{\rho_0\Delta y^2}D_V{}^{n+1}_{ij+1}, \tag{30}$$

$$E^{n+1}_{ijk}=\frac{\Delta t}{\rho_0\Delta\sigma_k\Delta\tilde{\sigma}_{k-1}D^{n+1}_{ij}}, \tag{31}$$

$$F^{n+1}_{ijk}=\frac{\Delta t}{\rho_0\Delta\sigma_k\Delta\tilde{\sigma}_kD^{n+1}_{ij}}, \tag{32}$$

$$G^{n+1}_{ijk}=-(A^{n+1}_{ijk}+B^{n+1}_{ijk}+C^{n+1}_{ijk}+D^{n+1}_{ijk}+E^{n+1}_{ijk}+F^{n+1}_{ijk}). \tag{33}$$

This is an elliptic equation in p, which is solved using an iterative method. In this implementation we use the BiCGSTAB iteration method (Barrett et al., 1994).

If p is ordered into a vector, Eq. (26) can be written compactly in matrix form as

$$Ap^{n+1,v}=b+Cp^{n+1,v-1}, \tag{34}$$

where A is a banded matrix, b represents the lack of volume conservation in the fields U^{n*}_{ADV}, V^{n*}_{ADV}, w^n, η^n, and η^{n+1}. $Cp^{n+1,v-1}$ represents the terms involving the velocity corrections U_{CORR2} and V_{CORR2}. In order to minimise roundoff errors, we subtract the vector Ap^n from both sides of the equation before starting the iterations. The resulting system is then

$$A\mathrm{d}p^{n+1,v}=(b-Ap^n)+Cp^{n+1,v-1}, \tag{35}$$

which is solved for $\mathrm{d}p^{n+1,v}$, where $\mathrm{d}p^{n+1,v}=p^{n+1,v}-p^n$.

In many simulations, Δx and Δy can be much larger than $\Delta\sigma$. In these cases, the coefficients E and F will be much larger than the coefficients A,B,C, and D, causing a badly conditioned problem. A rescaling of the pressure of the form $p(x,y,\sigma)=\tilde{p}(x,y,\alpha\sigma)$ with a constant α, may therefore speed up the iterations. All terms involving $\partial p/\partial\sigma$ must then be multiplied by α. For example Eq. (25) turns into

$$\frac{w^{n+1}_{ijk}-w^n_{ijk}}{\Delta t}+\frac{r^{n+1}_{ijk}-r^{n*}_{ijk}}{\Delta t}=-\frac{\alpha}{D^{n+1}_{ij}\rho_0}\frac{\tilde{p}^{n+1}_{ijk-1}-\tilde{p}^{n+1}_{ijk}}{\Delta\tilde{\sigma}_{k-1}} \tag{36}$$

and the terms E and F are mapped the following way:

$$E\mapsto\alpha E, \tag{37}$$

$$F\mapsto\alpha F. \tag{38}$$

The choice $\alpha=\Delta\sigma^2D^2/\Delta x^2$ will in the case of constant distance between σ-layers and $\Delta x=\Delta y$ give coefficients in the pressure iterations that are everywhere of the same magnitude. In the current studies with variable layer thickness, the α was chosen as $\min(\Delta\sigma)^2\max(D)^2/\Delta x^2$. No systematic study of the best choice for the α value for this case has been performed.

The boundary condition for p is

$$\frac{\partial p}{\partial n}=0, \tag{39}$$

which implies that the pressure correction should cause no flux change across boundaries. An application of the Green's theorem shows that with this boundary condition, a necessary condition for the system of equations to be solvable is that the integral of the right-hand side of Eq. (26) over the domain is zero (Folland, 1995). This is the case here, since the depth integrated gradient of the horizontal velocities exactly balances the

change in surface elevation, and w and r are zero at the free surface and at the bottom, so the integrals of their derivatives are zero.

It should be noted that the Poisson problem with the Neumann boundary condition does not determine the solution uniquely. The solution is only determined up to an additive constant. This is not a real problem, since we are only interested in the gradient of the pressure. The problem can be solved by subtracting the mean pressure in each iteration or fixing the pressure at a given point. We have chosen the former solution in this implementation.

3.1. Further discussion on the implementation

In the current ocean model, there are two sets of horizontal velocities, called $U_{\mathrm{ADV}}, V_{\mathrm{ADV}}$ and U, V. The first set of velocities are computed after the depth averaged velocities are computed. They have the same depth integrated transport as the depth averaged velocities, and the same vertical variation as the velocities U, V. They are exactly volume conserving (to machine precision) and can therefore be used for advection. If the velocity corrections caused by the non-hydrostatic pressure are added to U_{ADV} and V_{ADV} without convergence in the pressure iteration to machine accuracy, we might introduce artificial divergence in the velocity fields and have associated problems with mass conservation and stability problems. An option may be to add the velocity corrections only to the total velocities U and V, since these velocities are not used for advection. This will however decrease the effect of the velocity correction, since the immediate effect of the non-hydrostatic correction on the advection will become indirect. In the 2D test cases to be discussed in Section 4, the velocity corrections were added to U_{ADV} and V_{ADV}. This was feasible since convergence to machine accuracy in the pressure iterations was achieved relatively quickly. It is still an open question whether this is feasible in more realistic domains. Another possibility which has not been tested yet is to adjust η if convergence of the non-hydrostatic pressure to machine accuracy has not been achieved.

3.2. The advection of the vertical velocity

The horizontal velocities are advected with a TVD scheme with a superbee limiter (Yang and Przekwas, 1992). This is a non-oscillating scheme with little numerical diffusivity. It was therefore chosen to advect the new prognostic vertical velocity with the same scheme. Transforming the total derivative of the vertical velocity W to σ-coordinates, shows that it is the velocity W that should be advected. It therefore seems natural first to transform the vertical velocity w into the W vertical velocity using Eq. (19), and then advect this velocity before transforming back into a new w-velocity. It is important that this is done after the advection of scalars and horizontal velocities, since this operation may introduce divergence in the velocity field.

4. The test cases

When a dense fluid is released in a less dense ambient fluid, the dense fluid will spread under the influence of its buoyancy, with a distinct raised head followed by a shallower flow behind. Motions of this kind are often referred to as gravity currents or density currents, and have been studied over a number of years. When the flow is along a horizontal boundary, the head is a controlling feature of the flow. Britter and Simpson (1978) and Simpson and Britter (1979) have shown how the mixing, which occurs immediately behind the head, determines the rate of advance of the current.

According to Simpson (1987) the motion of a gravity current down a slope is appreciably different from that along a horizontal surface. Britter and Linden (1980) states that for gravity currents flowing down an incline there can be balance between the gravitational force and the frictional and entrainment drag. As a consequence the flow is steady. On the other hand, for horizontal current the frictional and entrainment drag will inevitable decrease the current velocity.

Ellison and Turner (1959) investigated the motion of a gravity current, and in particular the

entrainment into the current. It was shown that for the continuous current well behind the head, the mean velocity down the slope was independent of the downstream distance from the source. The thickness of the current, however, increased downstream due to entrainment, maintaining a constant buoyancy flux down the slope.

Britter and Linden (1980) restricted their attention to the case of large Reynolds numbers and unstratified ambient water. Their experimental results showed that

- For very small slopes (slope angle $\leqslant 0.5^\circ$) the head decelerates with distance from the source. At greater slopes the buoyancy force is large enough to overcome frictional effects and a steady head velocity results.
- For a Boussinesq plume the front velocity is found to be approximately 60% of the mean velocity of the following flow. This means that the head increases in size as it travels down the slope, both by direct entrainment into the head itself and by addition of fluid from the following flow. Direct entrainment increases with increasing slope and accounts for one-tenth of the growth of the head at 10° and about two-thirds at 90°.
- The velocity of the front show small variations with the slope angle. The gravitational force increase with slope, but so do entrainment, both into the head itself and the flow behind. This produces an increased retarding force on the current as momentum is imparted to the entrained fluid.

In the first test case, there is no ambient stratification, so the above theory can be applied directly. The second test case includes stratification, which will inevitably slow down the flow as it reaches the level of equal density.

4.1. Test case 1

The first test case is identical to the problem proposed in Haidvogel and Beckmann (1999, Chapter 6.4). A 2D idealised slope with horizontal dimension $0 \leqslant x \leqslant 200$ km is specified using a tanh-profile

$$h(x) = H_{\min} + \frac{1}{2}(H_{\max} - H_{\min}) \times (1 + \tanh((x - x_0)/L_S)), \quad (40)$$

where $H_{\min} = 200$ m, $H_{\max} = 4000$ m, $L_S = 10$ km, and $x_0 = 100$ km. This gives a maximum slope angle of about 10°. A density front is located at $x = 60$ km, with a density of 1030 and 1025 kg m^{-3} to the left and right of the front, respectively, see Fig. 2. The initial velocity field is at rest. The left and right boundaries are open boundaries, using the FRS open boundary relaxation technique (Martinsen and Engedahl, 1987).

In Haidvogel and Beckmann (1999) this case is run with different numerical models and with different schemes for the parameterisation of subgrid-scale processes. The results were seen to be sensitive both to the model used and to the subgrid-scale parameterisation.

An effect not studied in Haidvogel and Beckmann (1999), is the sensitivity to non-hydrostatic effects. They state in a footnote that non-hydrostatic effects probably are important, because of the large vertical velocities. In our simulations, the horizontal resolution is 500 m. The vertical resolution was increased until no significant changes could be seen in the solution, and in these simulations 70 layers are used, with increased resolution near the bottom. The σ-values at the cell interfaces are as follows: 0.000, −0.041, −0.081,

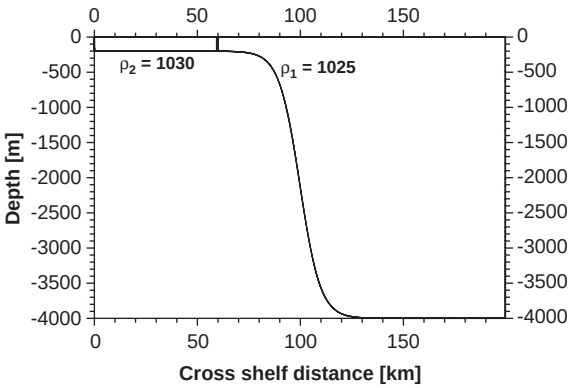

Fig. 2. The initial setup for test case 1.

−0.120, −0.158, −0.194, −0.230, −0.265, −0.298, −0.331, −0.362, −0.393, −0.422, −0.450, −0.477, −0.504, −0.529, −0.553, −0.576, −0.598, −0.619, −0.638, −0.657, −0.675, −0.692, −0.707, −0.722, −0.735, −0.748, −0.759, −0.769, −0.779, −0.787, −0.794, −0.800, −0.806, −0.811, −0.817, −0.822, −0.828, −0.833, −0.839, −0.844, −0.850, −0.856, −0.861, −0.867, −0.872, −0.878, −0.883, −0.889, −0.894, −0.900, −0.906, −0.911, −0.917, −0.922, −0.928, −0.933, −0.939, −0.944, −0.950, −0.956, −0.961, −0.967, −0.972, −0.978, −0.983, −0.989, −0.994, −1.000. Sensitivity to the vertical resolution is investigated in Vikebø et al. (2001). In this study it is shown that when increasing the number of σ-layers from 50 to 70 with focus towards the bottom, the shape of the density plume is better preserved down the slope.

The hydrostatic results in Fig. 3 look quite similar to results obtained in Haidvogel and Beckmann (1999) (Fig. 6.12 in Haidvogel and Beckmann, 1999), with respect to propagation speed and shape of the plume-head. The non-hydrostatic results, however, in Fig. 4, show a plume that is more localised in space, and the density of the plume head is well preserved as the plume descends. The height of the plume head grows as the plume descends, in accordance with the theory in Britter and Linden (1980). The contour plots of speed in Fig. 5, also illustrate this; a distinct head can be seen in the non-hydrostatic case, in accordance with theory. The internal speed of the head is higher than the following flow, but the propagation speed is lower. In the hydrostatic case the head is not as distinct, and there is also a pressure wave propagating in the entire water column.

The value of the density along the bottom is plotted against time in Hovmöller diagrams, Fig. 6. These diagrams clearly show that the density gradient at the head of the plume is better preserved in the non-hydrostatic case. These diagrams also make it easy to read the advancement speed of the head. The advancement speed can be seen to vary slightly as a function of slope angle, with an average speed of about 1.8 m s^{-1} in the hydrostatic case and 2.1 m s^{-1} in the non-

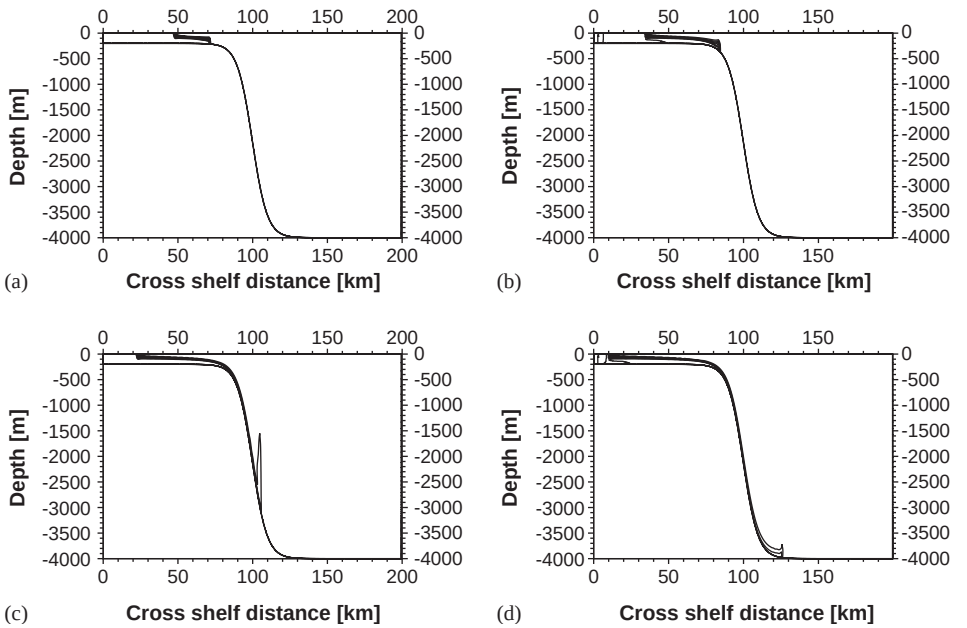

Fig. 3. Time development of the density distribution (kg m^{-3}) for the unstratified hydrostatic case, 0.5 kg m^{-3} between contour lines. (a) 2.5 h, (b) 5 h (c) 7.5 h (d) 10 h.

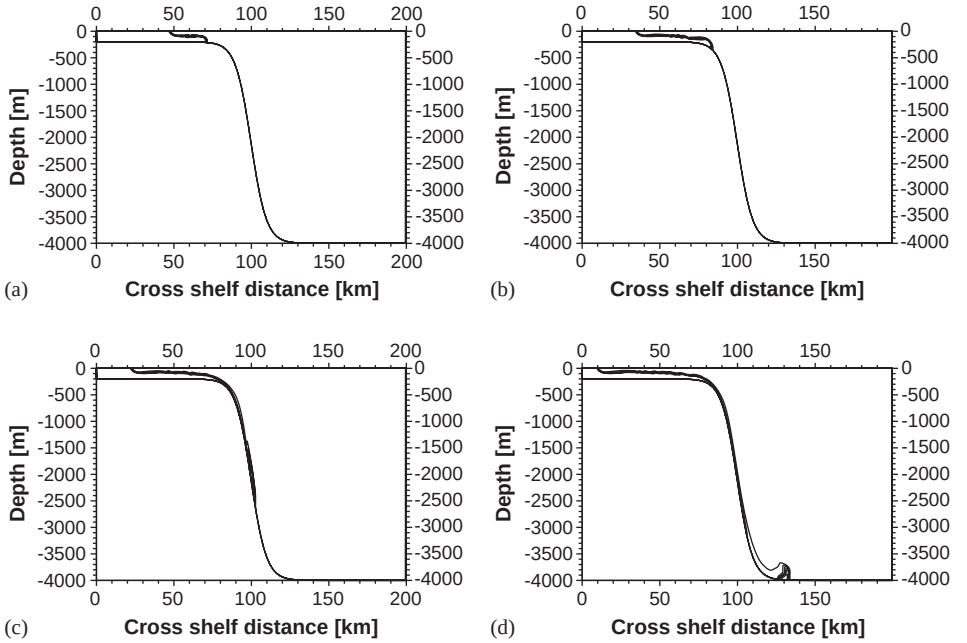

Fig. 4. Time development of the density distribution ($kg\,m^{-3}$) for the unstratified non-hydrostatic case, $0.5\,kg\,m^{-3}$ between contour lines. (a) 2.5 h, (b) 5 h (c) 7.5 h (d) 10 h.

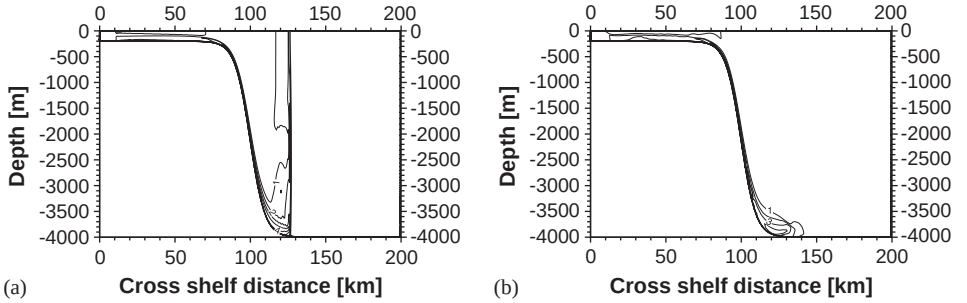

Fig. 5. Contour plots of the speed ($m\,s^{-1}$) after 10 h in the hydrostatic and non-hydrostatic case, $1\,m\,s^{-1}$ between contour lines. (a) Hydrostatic case, (b) Non-hydrostatic case.

hydrostatic case. In both cases the advancement speed is less than the mean speed of the following flow, as in the experimental results by Britter and Linden (1980).

4.2. Test case 2

This test case is similar to test case 1, but the bottom topography is an idealisation of the shelf slope off mid-Norway, as proposed in Ommundsen (2000)

$$h(x) = \begin{cases} H_{\min} & 0 \leqslant x \leqslant L_S \\ H_{\max} - (H_{\max} & \\ \quad -H_{\min})\left(\frac{L_L - x}{L_L - L_S}\right)^2 & L_S < x < L_L \\ H_{\max} & L_L \leqslant x \leqslant L, \end{cases} \tag{41}$$

where $H_{\min} = 250\,m$, $H_{\max} = 1300\,m$, $L_S = 60\,km$, $L_L = 160\,km$ and $L = 200\,km$. This implies an average slope angle of about 1°.

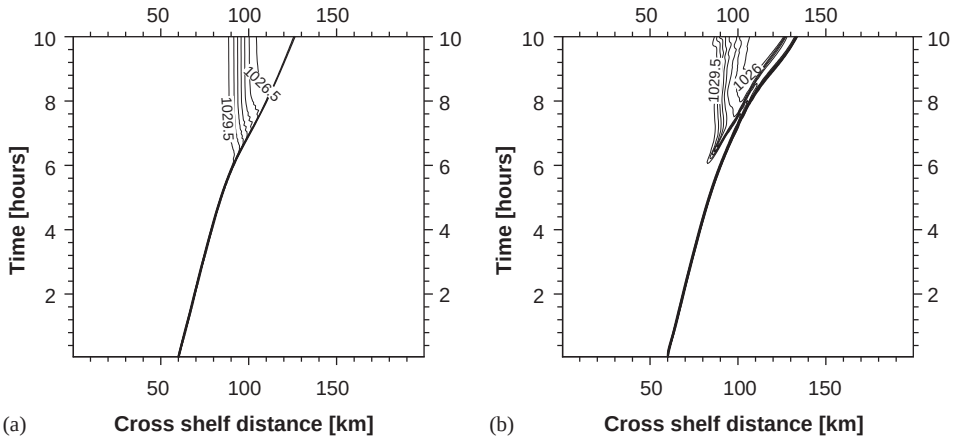

Fig. 6. Hovmöller diagrams of the bottom density ($kg\,m^{-3}$) for test case 1, $0.5\,kg\,m^{-3}$ between contour lines. (a) Hydrostatic case, (b) Non-hydrostatic case.

The stratification is taken from climatology (Engedahl et al., 1998), and is for simplicity chosen to be horizontally uniform. Model studies with a horizontal resolution of 400 m indicate that water from about 750 m may run up the shelf slope and onto the shelf during strong wind events, see Eliassen et al. (2000). This dense water may subsequently flow down the shelf slope. To study the processes during this phase, water with density corresponding to the initial density at 750 m depth (about $1028.1\,kg\,m^{-3}$) is elevated up to the shelf as a 50 m thick layer. The ambient density at the shelf edge level is about $1027.5\,kg\,m^{-3}$. The initial velocity field is at rest. The left and right boundaries are open boundaries, using the FRS open boundary relaxation technique (Martinsen and Engedahl, 1987).

The bottom topography and initial density distribution can be seen in Fig. 7. To highlight the plume, the density contours are especially dense in the interval 1027.5–$1028.1\,kg\,m^{-3}$.

The horizontal resolution is 500 m, and 70 layers are used in the vertical, with the same distribution as in test case 1.

As the plume flows down the slope, the density difference between the plume and the surrounding water will decrease, both because the plume moves towards a level of equal density, but also because of entrainment. The plume is therefore expected to find a new level of neutral buoyancy above the level where the water was initially taken from.

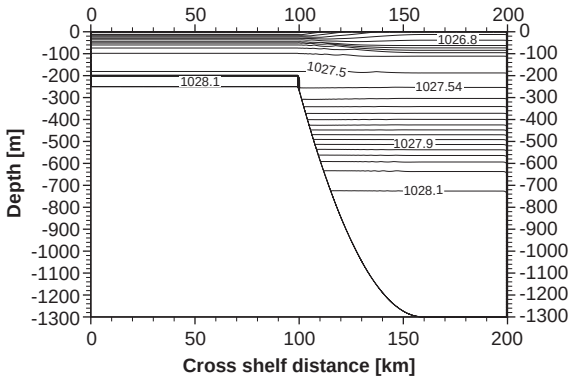

Fig. 7. Bathymetry and initial density distribution for test case 2. The distance between the density contours is $0.2\,kg\,m^{-3}$ for density less than $1027.0\,kg\,m^{-3}$, $0.1\,kg\,m^{-3}$ for density between 1027.0 and $1027.5\,kg\,m^{-3}$, and $0.04\,kg\,m^{-3}$ for density higher than $1027.5\,kg\,m^{-3}$.

The time development of the plume is shown in Figs. 8 and 9. There is a slight zoom-in in order to focus on the plume. As in the unstratified case, the plume head is better developed in the non-hydrostatic case. The head also grows in height and length as the gravity current travels down slope, although the head vanishes as it reaches the level of neutral buoyancy.

The hydrostatic simulations give no clear plume head, except possibly in the very early stages of the

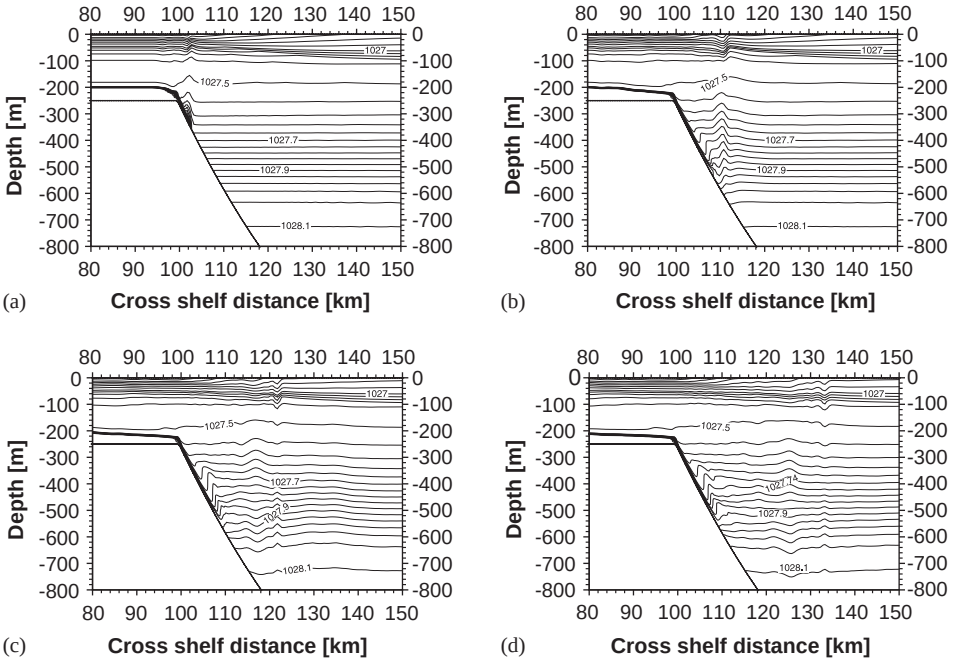

Fig. 8. Time development of the density distribution ($kg\,m^{-3}$) for the hydrostatic case 2. (a) 2 h, (b) 8 h, (c) 14 h, (d) 20 h.

flow. There is a very clear barotropic wave caused by the sudden release of the density front. Such a wave is also apparent in the non-hydrostatic simulations, but it is not as pronounced. We believe that the reason for this is that more of the energy goes to local adjustments of the velocities in the non-hydrostatic case, so less energy is available for conversion into barotropic kinetic energy. The propagation speed of the wave is about $2\,m\,s^{-1}$, which fits well with the speed of internal gravity waves.

The Hovmöller diagrams in Fig. 10 also show that the density of the plume head is better preserved in the non-hydrostatic case, allowing the head to travel further. It takes longer time to build up the momentum in the non-hydrostatic case, but once the gravity current starts travelling down slope, the propagation speed is about the same as in the hydrostatic case.

Fig. 11, shows the development of horizontal speed at the shelf edge and some positions off the shelf edge. The velocities in the hydrostatic case exhibit some periodic oscillations, which are probably due to the internal wave generated in this case. The velocity 2 km off the shelf edge has the highest maximum of about $0.75\,m\,s^{-1}$ in this case. This differs from the non-hydrostatic simulations, where the velocity at the shelf edge has the highest maximum (about $0.9\,m\,s^{-1}$). After the time of maximum speed level at the shelf edge, the speed at this point in the non-hydrostatic case is approximately twice as large as in the hydrostatic case. The oscillations in the non-hydrostatic case are not as smooth and periodic as in the hydrostatic case.

5. Discussion

The validity of the hydrostatic assumption made in many ocean models becomes questionable for phenomena involving large vertical speed variations and for many small scale phenomena, especially when the stratification is weak. This report explains a way to extend a hydrostatic σ-coordinate ocean model to include non-hydrostatic physics. Non-hydrostatic effects are important when studying density currents. If the model

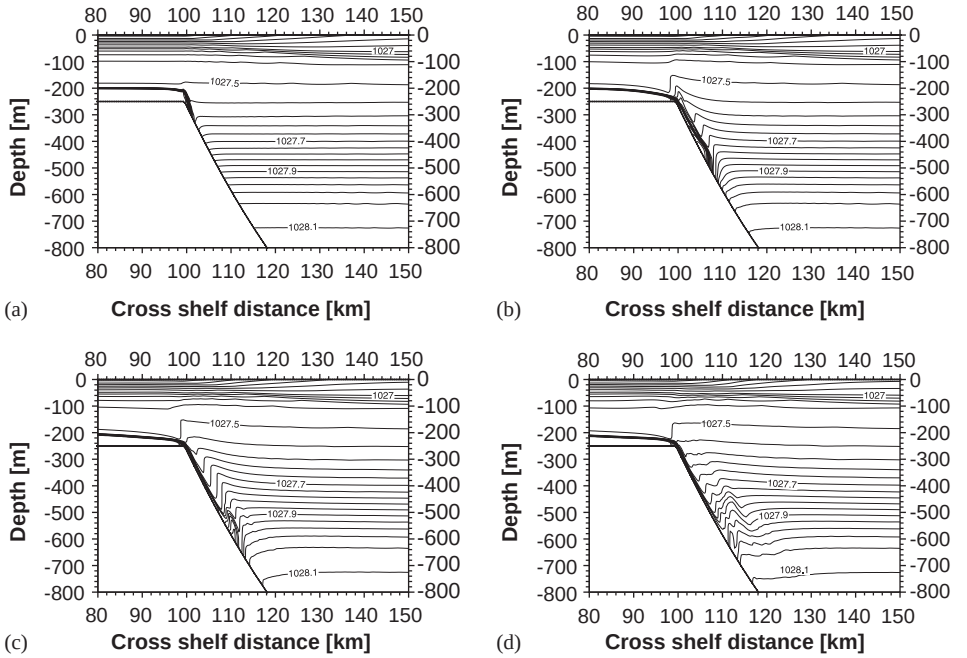

Fig. 9. Time development of the density distribution ($kg\,m^{-3}$) for the non-hydrostatic case 2. (a) 2 h, (b) 8 h, (c) 14 h, (d) 20 h.

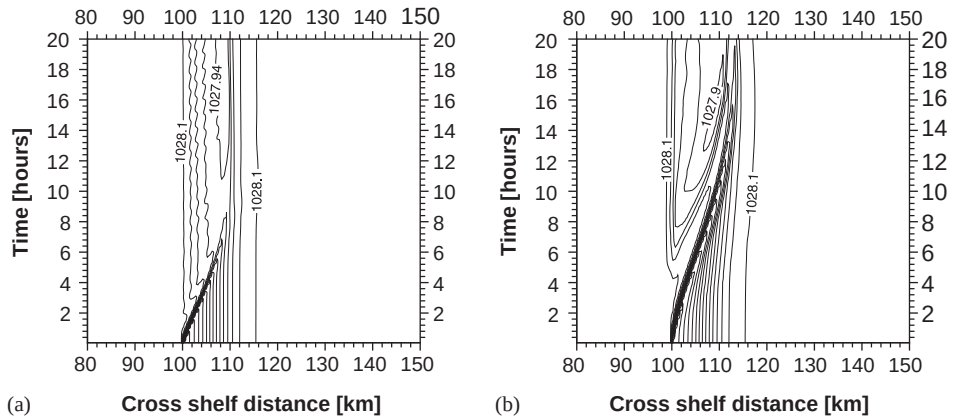

Fig. 10. Hovmöller diagrams of the bottom density ($kg\,m^{-3}$) for test case 2. (a) Hydrostatic case, (b) Non-hydrostatic case.

in addition is terrain following, the near sea bed layer and the processes in this layer may also be well resolved. The equations for the non-hydrostatic pressure in a σ-coordinate model may, as described in this paper, become more complicated than the corresponding equations for a z-coordinate model. Simplifications of the present strategy should therefore be sought.

The solution of the elliptic pressure equation is very expensive, and accounts for at least half the computing time on the test cases presented here. We believe improvements are possible, for example by using better pre-conditioners.

Substantial differences are seen between the hydrostatic and non-hydrostatic simulations of gravity plumes both in unstratified and stratified

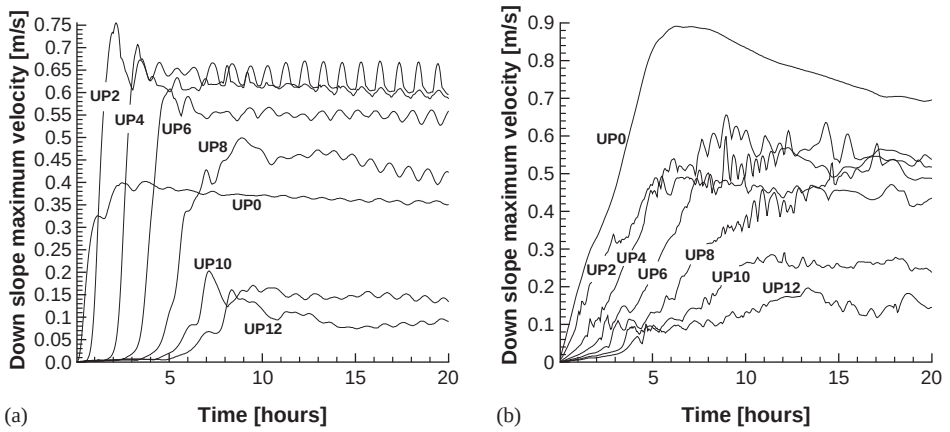

Fig. 11. The maximum velocity in the water columns at stations 0, 2, 4, 6, 8, 10 and 12 km off the shelf edge in the hydrostatic and non-hydrostatic case. (a) Hydrostatic case, (b) Non-hydrostatic case.

ambient water. In the non-hydrostatic simulations the density contrast at the plume head is better preserved, and the plume height and length grows as the plume advances in accordance with theory.

The test cases described in the present paper are two-dimensional. In three dimensions it will become more expensive to solve the pressure equations. Also the pressure corrections driven by horizontal divergence may affect the horizontal flow rather than the vertical velocities. At present it is not clear how this will affect the non-hydrostatic pressure corrections.

In the real ocean, the flow of dense water down steep topography will be strongly influenced by the earths rotation. Overflows has recently been studied with a $1\frac{1}{2}$-layer model in Shapiro and Hill (1997). In Jiang and Garwood Jr. (1996) the POM is used to study overflows, and Shi et al. (2001) used an isopycnal model to study variability of the Denmark Strait overflow. These studies are performed with models using the hydrostatic approximation. There is also a considerable interest in boundary layer mixing along the continental slopes and along the shelf edges, see Munk and Wunsch (1998). The breaking of internal waves may explain the enhanced mixing in these regions. Internal waves and the reflection of the waves are also influenced by the earths rotation, see Thorpe (2000). In several studies models have been applied to investigate internal tides and their interaction with topography, see for instance Xing and Davies (2001, 2002); Davies and Xing (2002). Most of these studies are performed with hydrostatic models. In Legg and Adcroft (2003), however, the non-hydrostatic MIT model, see Marshall et al. (1997a) is used to study internal wave dynamics, and significant differences between hydrostatic and non-hydrostatic results are described. The spatial variability near the sea-bed is high both horizontally and vertically. Recent analysis of high frequency measurements also show that the temporal variability in the bottom boundary layer may be very high, see Hosegood and van Haren (2003).

There is thus a need for 3D non-hydrostatic models with high resolution, in time and space, to facilitate studies of processes along the continental slopes. The effects of rotation must be included. The vertical resolution near the sea-bed should be high enough to allow the representation of for instance density plumes and/or internal bores. Terrain following 3D models with non-hydrostatic capabilities should be adequate for such studies. The model presented in this paper may be regarded as a step on the way towards such a model.

Acknowledgements

This research has received support from The Research Council of Norway through the strategic university program *On Basic Problems Related to Numerical Simulations in Fluid Dynamics* and through a grant of computing time (Programme for Supercomputing). This work was also supported by Norsk Hydro Grant NHT-B44-5098606-00 and Grant NH-5203909. Two anonymous referees are thanked for useful remarks.

References

Avlesen, H., Berntsen, J., Espelid, T., 2001. A convergence study of two prognostic, sigma coordinate ocean models on a density driven flow in a quadratic basin. International Journal of Numerical Methods in Fluids 36, 639–657.

Barrett, R., Berry, M., Chan, T., Demmel, J., Donato, J., Dongarra, J., Eijkhout, V., Pozo, R., Romine, C., Van der Vorst, H., 1994. Templates for the Solution of Linear Systems: Building Blocks for Iterative Methods. SIAM, Philadelphia.

Berntsen, J., 2000. USERS GUIDE for a modesplit σ-coordinate numerical ocean model. Technical Report 135, Department of Applied Mathematics, University of Bergen, Johs. Bruns gt.12, N-5008 Bergen, Norway, 48p.

Berntsen, J., 2002. Internal pressure errors in sigma-coordinate ocean models. Journal of Atmospheric and Oceanic Technology 19 (9), 1403–1414.

Berntsen, J., Svendsen, E., 1999. Using the Skagex dataset for evaluation of ocean model skills. Journal of Marine Systems 18, 313–331.

Berntsen, H., Kowalik, Z., Sælid, S., Sørli, K., 1981. Efficient numerical simulation of ocean hydrodynamics by a splitting procedure. Modeling Identification and Control 2, 181–199.

Blumberg, A., Mellor, G., 1987. A description of a three-dimensional coastal ocean circulation model. In: Heaps, N. (Ed.), Three-Dimensional Coastal Ocean Models. Coastal and Estuarine Series, Vol. 4. American Geophysical Union, p. 208.

Britter, R., Linden, P., 1980. The motion of the front of a gravity current travelling down an incline. Journal of Fluid Mechanics 99, 531–543.

Britter, R., Simpson, J., 1978. Experiments on the dynamics of a gravity current head. Journal of Fluid Mechanics 88, 223–240.

Davies, A., Xing, J., 2002. Models of near-bed dynamics and sediment movement at the Iberian margin. Progress in Oceanography 52, 373–397.

Dudhia, J., 1993. A nonhydrostatic version of the Penn State-NCAR mesoscale model: Validation tests and simulation of an Atlantic cyclone and cold front. Monthly Weather Review 121, 1493–1511.

Eliassen, I., Eldevik, T., Berntsen, J., Furnes, G., 2000. The current conditions at Ormen Lange-Storegga. Technical Report, Department of Applied Mathematics, University of Bergen, Johs. Bruns gt.12, N-5008 Bergen, Norway, 22p.

Eliassen, I., Heggelund, Y., Haakstad, M., 2001. A numerical study of the circulation in Saltfjorden, Saltstraumen and Skjerstadfjorden. Continental Shelf Research 21, 1669–1689.

Ellison, T., Turner, J., 1959. Turbulent entrainment in stratified flow. Journal of Fluid Mechanics 6, 423–448.

Engedahl, H., Ådlandsvik, B., Martinsen, E., 1998. Production of monthly mean climatological archives of salinity, temperature, current and sea level for the Nordic Seas. Journal of Marine Systems 14, 1–26.

Folland, G., 1995. Introduction to Partial Differential Equation. Princeton University Press, Princeton, NJ.

Haidvogel, D., Beckmann, A., 1999. Numerical ocean circulation modeling. Series on Environmental Science and Management, Vol. 2. Imperial College Press.

Hosegood, P., vanHaren, H., 2003. Ekman-induced turbulence over the continental slope in the Faeroe-Shetland Channel as inferred from spikes in current meter observations. Deep-Sea Research I 50, 657–680.

Jiang, L., Garwood Jr., R., 1996. Three-dimensional simulations of overflows on continental slopes. Journal of Physical Oceanography 26, 1214–1233.

Kowalik, Z., Murty, T., 1993. Numerical Modeling of Ocean Dynamics. Advanced Series on Ocean Engineering, Vol. 5. World Scientific, Singapore.

Lamb, K., 1994. Numerical experiments of internal wave generation by strong tidal flow across a finite amplitude bank edge. Journal of Geophysical Research 99, 843–864.

Legg, S., Adcroft, A., 2003. Internal wave breaking at concave and convex continental slopes. Journal of Physical Oceanography 33, 2224–2246.

Legg, S., McWilliams, J., 2000. Temperature and salinity variability in heterogeneous ocean convection. Journal of Physical Oceanography 30, 1188–1206.

Legg, S., McWilliams, J., 2001. Convective modifications of a geostrophic eddy field. Journal of Physical Oceanography 31, 874–891.

Legg, S., McWilliams, J., Gao, J., 1998. Localization of deep ocean convection by a mesoscale eddy. Journal of Physical Oceanography 28, 944–970.

Mahadevan, A., Oliger, J., Street, R., 1996a. A Nonhydrostatic Mesoscale Ocean Model. Part I: Well posedness and scaling. Journal of Physical Oceanography 26, 1868–1880.

Mahadevan, A., Oliger, J., Street, R., 1996b. A Nonhydrostatic Mesoscale Ocean Model. Part II: Numerical implementation. Journal of Physical Oceanography 26, 1881–1900.

Marshall, J., Adcroft, A., Hill, C., Perelman, L., Heisey, C., 1997a. A finite-volume, incompressible Navier–Stokes model for studies of the ocean on parallel computers. Journal of Geophysical Research 102 (C3), 5753–5766.

Marshall, J., Hill, C., Perelman, L., Adcroft, A., 1997b. Hydrostatic, quasi-hydrostatic, and nonhydrostatic ocean

modeling. Journal of Geophysical Research 102 (C3), 5733–5752.

Martinsen, E., Engedahl, H., 1987. Implementation and testing of a lateral boundary scheme as an open boundary condition in a barotropic ocean model. Coastal Engineering 11, 603–627.

Mellor, G., 1996. Users guide for a three-dimensional, primitive equation, numerical ocean model. Technical Report, Princeton University.

Mellor, G., Yamada, T., 1982. Development of a turbulence closure model for geophysical fluid problems. Reviews of Geophysics and Space Physics 20, 851–875.

Mesinger, F., Arakawa, A., 1976. Numerical methods used in atmospheric models, Volume I. WMO/ICSU Joint Organizing Committee, Garp Publication Series No. 17.

Munk, W., Wunsch, C., 1998. Abyssal recipes II: energetics of tidal and wind mixing. Deep-Sea Research I 45, 1978–2010.

Ommundsen, A., 2000. Numerical simulations of tides, shelf slope currents and Lagrangian advection of particles. Ph.D. thesis, Department of Mathematics, University of Oslo, Norway.

Patankar, S., 1980. Numerical Heat Transfer and Fluid Flow. Series in Computational and Physical Processes in Mechanics and Thermal Sciences. Taylor & Francis, London.

Shapiro, G., Hill, A., 1997. Dynamics of dense water cascades at the shelf edge. Journal of Physical Oceanography 27, 2381–2394.

Shi, X., Røed, L., Hackett, B., 2001. Variability of the Denmark Strait overflow: a numerical study. Journal of Geophysical Research 106 (C10), 22277–22294.

Simpson, J., 1987. Gravity Currents in the Environment and the Laboratory. Halsted Press, New York.

Simpson, J., Britter, R., 1979. The dynamics of the head of a gravity current advancing over a horizontal plane. Journal of Fluid Mechanics 94, 477–495.

Smagorinsky, J., 1963. General circulation experiments with the primitive equations, I. The basic experiment. Monthly Weather Review 91, 99–164.

Stansby, P., Zhou, J., 1998. Shallow-water flow solver with non-hydrostatic pressure: 2D vertical plane problem. International Journal for Numerical Methods in Fluids 28, 541–563.

Thorpe, S., 2000. The effects of rotation on the nonlinear reflection of internal waves from a slope. Journal of Physical Oceanography 30, 1901–1909.

Vikebø, F., Berntsen, J., Furnes, G., 2001. Gravity currents at Ormen Lange. Technical Report 163, Department of Applied Mathematics, University of Bergen, Norway.

Xing, J., Davies, A., 2001. Non-linear effects of internal tides on the generation of the tidal mean flow at the Hebrides shelf edge. Geophysical Research Letters 28, 3939–3942.

Xing, J., Davies, A., 2002. Processes influencing the non-linear interaction between inertial oscillations, near inertial internal waves and internal tides. Geophysical Research Letters 29, 10.1029/2001GL014199.

Yang, H., Przekwas, A., 1992. A comparative study of advanced shock-capturing schemes applied to Burgers equation. Journal of Computational Physics 102, 139–159.